IEEE Access
Multidisciplinary ⋮ Rapid Review ⋮ Open Access Journal

Received 8 December 2023, accepted 22 December 2023, date of publication 28 December 2023, date of current version 5 January 2024.

Digital Object Identifier 10.1109/ACCESS.2023.3347797

RESEARCH ARTICLE

A Constant Voltage/Current CPT System With Lightweight Characteristics for the Unmanned Aerial Vehicle

YUFANG CHANG[1], XIAOKE ZHANG[1], CHAO MA[1], WENCONG HUANG[1], AND HUAICHENG YAN[2], (Senior Member, IEEE)

[1]Hubei Provincial Key Laboratory for Efficient Utilization and Energy Storage Operation Control of Solar Energy, Hubei University of Technology, Wuhan 430068, China

[2]School of Information Science and Engineering, East China University of Science and Technology, Shanghai 200237, China

Corresponding author: Yufang Chang (changyf@hbut.edu.cn)

This work was supported by the Opening Foundation Projects of Southern Power Grid Corporation Wireless Power Transmission Joint Laboratory under Grant GXKJXM20210149.

ABSTRACT The large weight of the unmanned aerial vehicle (UAV) could cause a decrease in endurance mileage, while poor anti-offset performance could extend charging time and may even damage onboard equipment. To address the above issues in constant-voltage/current capacitive power transfer (CPT) system for the UAV, a constant voltage/current (CV/CC) CPT system with lightweight characteristics for the UAV is proposed. Firstly, a capacitive coupler with strong anti-offset tolerance for the CPT system is proposed, and the coupling performance and equivalent model are studied. Secondly, the switching strategy for constant voltage/current output is studied based on the T-π type compensation circuit, without additional compensating elements. Finally, a simulation model and a test prototype are built to verify the feasibility and effectiveness of the proposed system. The results show that the system achieved a constant voltage output of 60 V and a constant current output of 2 A. And the rate of change of the output voltage and current is less than 6% when the capacitive coupler is offset by $\pm$100 mm, the rate of that is less than 6% when the load changes. The switching strategy proposed in this paper has obvious lightweight advantages and could serve as a reference for designing the CPT system for the UAV.

INDEX TERMS Capacitive power transfer (CPT), anti-offset, constant voltage, constant current, light weight.

I. INTRODUCTION

The capacitive couplers of Capacitive Power Transfer (CPT) system come in various forms, offering the advantages of minimal eddy current loss and a high tolerance for metallic foreign objects [1], [2], [3], [4], [5], [6], [7]. Therefore, the CPT system has found wide-ranging applications, encompassing areas like electric vehicles, unmanned aerial vehicles (UAVs), and implantable medical devices [8], [9], [10].

Wireless power transmission technology solutions could reduce the battery capacity requirements for UAVs, and extend their range, but they require constant voltage/current (CV/CC) charging and high offset tolerance [11], [12].

In inductive power transfer (IPT) system, a uniformly distributed magnetic field can be constructed to ensure that the magnetic flux does not change when the receiving coil is displaced, thereby improving the system's resistance to displacement [13]. However, due to the different transmission mechanisms between CPT and IPT systems, CPT systems often use other methods to improve displacement tolerance.

At present, the primary methods for improving the offset tolerance of capacitive couplers involve modifying the coupler's structure, such as using matrix-type emitter plates and specially shaped capacitive couplers. A reconfigurable capacitive coupler for UAVs was proposed in [14]. By adjusting the

The associate editor coordinating the review of this manuscript and approving it for publication was Alon Kuperman.

state of the emitter plate, it reduces the UAV's requirements for lateral, longitudinal, and rotational deviation. However, for this system to work, a communication link between the UAV and the wireless power transmitting side, as well as maintaining the relative positions of the receiving and transmitting plates, is necessary. A CPT system with strong offset tolerance and light-weight characteristics for UAVs was proposed in [15], which allow for ±90 mm offset in the x and y axes but does not account for rotational offset, but does not consider rotational offset. To address this limitation, additional compensation capacitance is required.

Compared to the approach of adding external controller and adjusting the system's operating frequency, the method of adding switches to change the constant voltage/current output stage of the system does not require additional detection circuit and control circuit, and it maintains system efficiency [16], [17]. A CPT system with two switches to change the constant current/voltage output stage was proposed in [18]. But the input impedance is not zero phase angle (ZPA), and the system topology is complex with a high order, and too many compensating components are used. A constant voltage/current electric field coupling power transmission system based on an F-F/T changeable resonant circuit was proposed in [19]. This system uses three switches and six compensating components. An electric-field coupled power transfer system with constant voltage/current output based on changeable LC-CLCL resonant circuit was proposed in [20]. This system uses two switches and five compensating components. However, they are not conducive to the system's state switching and lightweight. The above literature did not analyze the offset conditions of capacitive coupler, and use excessive compensating components, which could not meet the lightweight requirements of the system.

Considering the anti-offset performance of the UAV capacitive coupler, the requirement of constant voltage/current output and the weight limit, a lightweight CPT system of constant voltage/ current is proposed in this paper. This system uses fewer compensating components on the load side, which is beneficial for improving the lightweight performance of the system, increasing the payload capacity of drones, and extending the cruising distance of drones. Additionally, the system has strong anti-offset performance, which allows for an increase in the allowable error during landing while ensuring the rated charging voltage/current.

II. DESIGN OF CAPACITIVE COUPLER AND STUDY OF ANTI-OFFSET TOLERANCE

A. CAPACITIVE COUPLER STRUCTURE DESIGN

In this paper, an arch-slot capacitive coupler is proposed, as shown in Fig.1(a), and the 3D figure is shown in Fig.1(b). In Fig.1, P_1 and P_2 are the transmitting plates, P3 and P4 are the receiving plates, L_k represents the gap between the transmitting plates, which matches the distance between the receiving plates. L and H respectively denote the span and height of the arch structure.

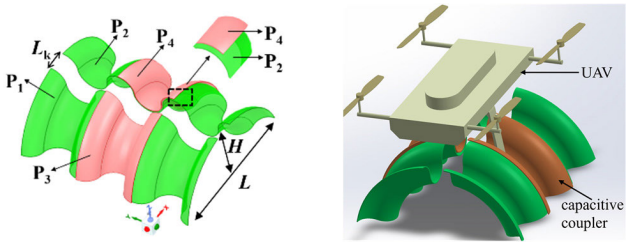

(a) Diagrammatic figure (b) 3D figure

FIGURE 1. Arch-slot capacitive coupler.

When the receiving plate is horizontally shifted along the x-axis, the relative position between the receiving plates and the transmitting plates is shown in Fig.2. In this case, there are three forces acting on the receiving plate, F_1, F_g and F_2. The force F_2 can be decomposed into two components: F_{2a}, perpendicular to the platform, and F_{2b}, parallel to the platform. Due to the presence of force F_{2b}, the UAV has a tendency to return to its right position like Fig.1, but it will be hindered by the frictional force F_{1b}. However, during the landing process of the UAV, the right side of the receiving plates will first come into contact with the transmitting plates, while the left side does not touch the platform. Therefore, there is no frictional force F_{1b}, and the UAV can complete position correction.

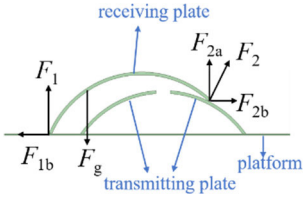

FIGURE 2. Force diagram of receiving plate.

When the receiving plate is in the extreme position, with one side of the receiving plates at the edge of the gap L_k of the transmitting plates, the relative position of the receiving plates and the transmitting plates is shown in Fig.3.

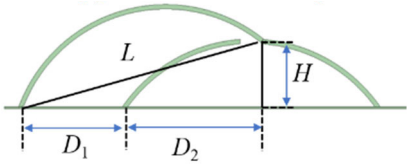

FIGURE 3. Relative position of the receiving and transmitting plates.

In the above situation, D_1 will determine the x-axis horizontal anti-offset capability of the capacitive coupler. D_1 satisfies:

$$(D_1 + D_2)^2 + H^2 = L^2 \tag{1}$$

Due to $D_2 = 0.5(L + L_k)$, formula (1) can be written as:

$$D_1 = \sqrt{L^2 - H^2} - 0.5(L + L_k) \tag{2}$$

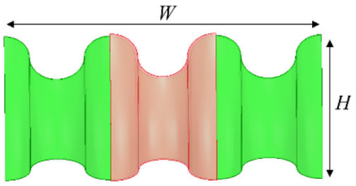

FIGURE 4. Side view of the capacitive coupler.

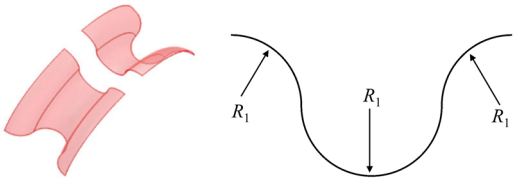

(a) Slot structure (b) Slot cross-section

FIGURE 5. The view of the slot.

The design of the slot structure enables the UAV to have anti-rotational offset capability. The side view is shown in Fig.4, where W is the length of the transmitting plates.

The slot structure is shown in Fig.5(a), and the section view of the slot structure is shown in Fig.5(b), where R_1 is the radius of the slot.

The principle of anti-rotational offset is: when the UAV experiences a rotational offset as shown in Figure 6(a) before landing, as long as the lowest points of the two receiving plates are within the same slot of the transmitting plates, it ensures that the receiving plates lands within the slot, and its maximum rotational offset situation is simplified as shown in Fig.6(b).

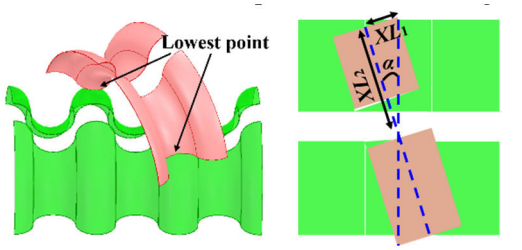

(a) Rotation offset diagram (b) Simplified diagram

FIGURE 6. The view of rotational situation.

The magnitude of the rotation offset angle α is:

$$\alpha = \arctan \frac{XL_1}{XL_2} \tag{3}$$

where, XL_1 is the width of a single slot, which is equal to $2R_1$, XL_2 is half the length of a single slot, which is equal to $L/2$, so α can be expressed as:

$$\alpha = \arctan \frac{4R_1}{L} \tag{4}$$

It can be seen from formula (4) that the maximum allowable rotational offset angle of this capacitive coupler is limited by the slot radius R_1 and the span of the arch structure L. Since L is determined by the size of the UAV, a larger R_1 will result in a larger rotational offset angle, but it will bring issues related to weight and air resistance. A smaller R_1 will allow for a smaller rotational anti-offset angle, resulting in poorer rotational anti-offset effectiveness.

B. DIMENSION STUDY OF CAPACITIVE COUPLER

Considering the current level of the UAV autonomous landing technology [21], the horizontal anti-offset range of this system should exceed ±50 mm, specifically D1⩾50 mm. The landing attitude angle must be greater than 5°, that is, the rotational anti-offset angle $\alpha \geqslant 5°$.

According to Fig.4 and Fig.5, the slot radius R_1 is affected by the number of slots N, and they satisfy:

$$R_1 = \frac{W}{4N} \tag{5}$$

In order to ensure the symmetry of the receiving plates, the number of slots is set to be odd. In this design, where W is 200 mm and L is 152 mm, the relationship between the number of slots, the radius of slots and the rotational anti-offset angle α is presented in Table.1.

TABLE 1. Parameters of slot.

Slot number	Slot radius/(mm)	α/(°)
3	16.7	±23.7
5	10.0	±14.7
7	7.1	±10.6

In order to reduce the landing precision requirements, this paper sets the rotational anti-offset angle α to 23.7°, resulting in a configuration with 3 slots and a slot radius of 16.7 mm.

According to formula (2), H is subject to L, L_k and D_1. When $D_1 \geqslant 50$ mm, H needs to satisfy:

$$H \leq \sqrt{L^2 - [50 + 0.5(L + L_k)]^2} \tag{6}$$

The relationship between the maximum value of H and L_k is shown in Fig.7.

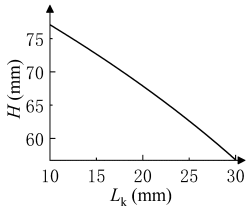

FIGURE 7. The maximum value of H and Lk curve graph.

From Fig.7, it can be seen that the maximum value of H and L_k are approximately inversely proportional. The smaller L_k is, the greater the range of selectable H, but it may lead to inter-plates voltage breakdown. On the other hand, a larger L_k can enhance the safety of the CPT system, but H will be lower, which might lead to the inability to install the

transmitting plates. Therefore, H must have sufficient margin when determining L_k.

According to Figure 5(b), When L_k ranges from 10 mm to 30 mm, H must exceed $2R_1$, which is 33.4 mm. To prevent inter-plates voltage breakdown and ensure that $D_1 \geqslant 50$ mm, L_k is chosen as 20 mm. So, D_1 is 54 mm, and the maximum value of H is 67.9 mm.

The dimensional parameters of the capacitive coupler are shown in Table.2.

TABLE 2. Parameters of capacitive coupler.

Parameters	Symbol	Value
Width of capacitive coupler	W	200 mm
Span of capacitive coupler	L	152 mm
Height of capacitive coupler	H	60 mm
Gap of capacitive coupler	L_k	20 mm
Radius of slot	R_1	16.7 mm
Number of slots	NULL	3

ANSYS Maxwell finite element simulation software is used to build the capacitive coupler model according to the data in Table.2, and its electric field distribution is shown in Fig.8

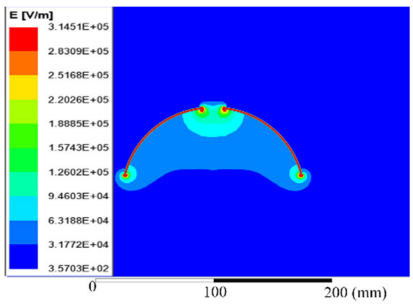

FIGURE 8. Electric field distribution of capacitive coupler.

As can be seen from Fig.8, the field strength at the center of the transmitting plates gap is about 9.45 × 10^4 V/m, which is smaller than the breakdown field strength of air at 3 × 10^6 V/m. It can be concluded that this capacitive coupler will not experience discharge phenomena, ensuring the safe of the system.

C. RESEARCH ON HORIZONTAL ANTI-OFFSET PERFORMANCE

In the actual CPT system, there are not only main coupling capacitance C_{13} and C_{24}, but also cross-coupling capacitance C_{12}, C_{14}, C_{23}, C_{34}, as shown in Fig.9.

According to Chapter II, Section B, the capacitive coupler consists of three slots, with each slot having a radius R_1 of 16.7mm. Therefore, the horizontal anti-offset distance on the y-axis is $\pm 6R_1$, which is equivalent to ±100mm When the UAV experiences a horizontal displacement along the y-axis,

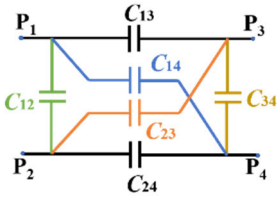

FIGURE 9. Six coupling capacitance model.

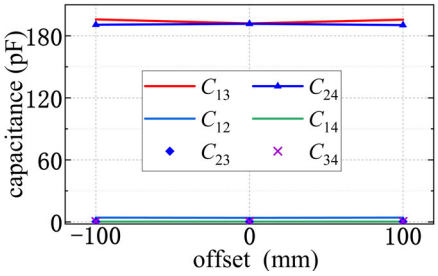

FIGURE 10. Variation diagram of coupling capacitance.

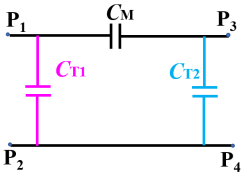

FIGURE 11. Model of three coupling capacitance.

the changes of coupling capacitance are depicted in Fig.10. When the UAV is not offset, its main coupling capacitance C_{13} and C_{24} are 192 pF and 191.6 pF respectively. When the UAV is offset by ±100 mm, the main coupling capacitance C_{13} is 194.8 pF and C_{24} is 192 pF respectively. That means the maximum variation of the main coupling capacitance is 1.46%. When the UAV's offset distance changes from 0 to ±100 mm, the cross-coupling capacitance C_{12} changes from 3.2 pF to 3.6 pF. While the other three cross-coupling capacitance, C_{14}, C_{23} and C_{34}, are all less than 0.5 pF in the three cases, and the variation amplitude is less than 0.1 pF.

It can be seen from the above that when the y-axis offset of the capacitive coupler occurs within ±100 mm, the value of each coupling capacitance basically does not change.

D. CROSS-COUPLING CAPACITANCE RESEARCH

In order to facilitate the analysis of the equivalent model of coupling capacitance, Fig.9 is simplified to the three-coupling capacitance model shown in Fig.11 [22].

In Fig.11, C_{T1} is the transmitting side's self- capacitance, C_{T2} is the receiving side's self- capacitance, and C_M is the

mutual capacitance, and they satisfy:

$$\begin{cases} C_{T1} = C_{12} + \dfrac{C_{13}C_{23} + C_{14}C_{24}}{C_{13} + C_{14} + C_{23} + C_{24}} \\ C_M = \dfrac{C_{13}C_{24} - C_{14}C_{23}}{C_{13} + C_{14} + C_{23} + C_{24}} \\ C_{T2} = C_{34} + \dfrac{C_{13}C_{14} + C_{23}C_{24}}{C_{13} + C_{14} + C_{23} + C_{24}} \end{cases} \tag{7}$$

Taking the obtained values of the coupling capacitors from Chapter II, Section B and plugging them into formula (6), we have $C_{\mathrm{M}} = 96$ pF, $C_{\mathrm{T1}} = 3.8$ pF, $C_{\mathrm{T2}} = 0.7$ pF. Since C_{T1} and C_{T2} are relatively much smaller than C_{M}. Therefore, in practical use, C_{T1} and C_{T2} can be neglected.

III. RESEARCH ON CONSTANT VOLTAGE/CURRENT OUTPUT CHARACTERISTICS

A. CPT SYSTEM CIRCUIT

The constant voltage/constant current output switching strategy is based on a π compensation circuit, which adjusts the two states of the π compensation circuit by adding two switches. These two states are the π state and the short-circuit state.

The CPT system circuit with constant voltage/current output is shown in Fig.12. The transmitting side of the system is composed of DC voltage source, inverter and T-LCL compensation circuit. The coupling unit is composed of C_{S1} and C_{S2}. The receiving side consists of a π-type compensation circuit, switches, rectification and filtering units, and a load resistor.

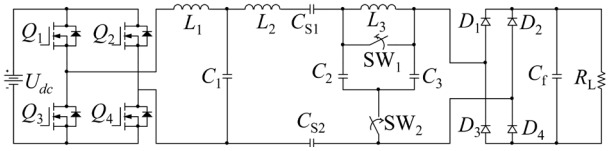

FIGURE 12. The circuit of the CPT system.

Fig.12 can be simplified as Fig.13. Based on the fundamental frequency analysis method, the DC voltage source and the inverter circuit can be represented by an equivalent AC voltage source U_{in}. The equivalent coupling capacitance of the coupling unit is represented by C_{M}. Rectification, filtering, and the load are represented by the equivalent load R. The compensation inductance L_2 on the transmitting side is represented as $L_{2\mathrm{a}}$ and $L_{2\mathrm{b}}$ in series. T_1 constitutes the transmitting side compensation circuit, consisting of L_1, C_1, and $L_{2\mathrm{a}}$. The inductance $L_{2\mathrm{b}}$ in part T_2 is used to compensate for the coupling capacitance C_{M}. T_3 is the receiving-side compensation circuit, consisting of L_3, C_2, C_3, and two switches, SW_1 and SW_2.

In Fig.13, the effective value of U_{in}, equivalent load of R value, $L_{2\mathrm{a}}$ and $L_{2\mathrm{b}}$, they satisfy:

$$\begin{cases} U_{\mathrm{in}} = 2\sqrt{2}U_{dc}/\pi \\ R = \dfrac{8}{\pi^2}R_L \\ L_2 = L_{2a} + L_{2b} \end{cases} \tag{8}$$

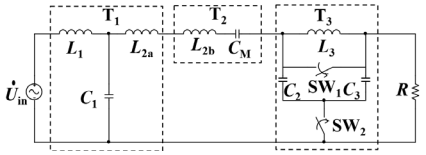

FIGURE 13. Simplified circuit of CPT system.

B. RESEARCH ON CONSTANT CURRENT OUTPUT CHARACTERISTICS

When switch SW_1 is closed and SW_2 is open, the components C_2 and C_3, along with L_3, will be shorted, as depicted in Fig. 14.

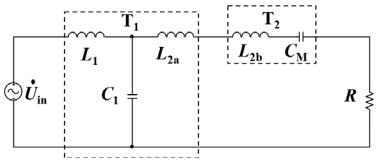

FIGURE 14. Constant current circuit.

To compensate C_{M}, the $L_{2\mathrm{b}}$ satisfies:

$$j\omega L_{2b} + \frac{1}{j\omega C_M} = 0 \tag{9}$$

According to formula (9), the impedance of T_2 is zero, so Fig.14 can be simplified to Fig.15.

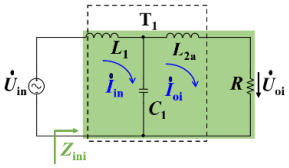

FIGURE 15. Simplified constant current circuit.

In Fig15, when the components included in T_1 satisfy formula (9), it can convert the constant input voltage U_{in} into a constant output current while satisfying the ZPA state.

$$\begin{cases} j\omega L_1 + \dfrac{1}{j\omega C_1} = 0 \\ j\omega L_{2a} + \dfrac{1}{j\omega C_1} = 0 \end{cases} \tag{10}$$

According to Kirchhoff's voltage law, the circuit shown in Fig.15 can be written as:

$$\begin{cases} \dot{U}_{\mathrm{in}} = \left(j\omega L_1 + \dfrac{1}{j\omega C_1}\right)\dot{I}_{\mathrm{in}} - \dfrac{1}{j\omega C_1}\dot{I}_{\mathrm{oi}} \\ 0 = -\dfrac{1}{j\omega C_1}\dot{I}_{\mathrm{in}} + \left(j\omega L_{2a} + R + \dfrac{1}{j\omega C_1}\right)\dot{I}_{\mathrm{oi}} - \dot{U}_{\mathrm{oi}} \end{cases} \tag{11}$$

In constant current output mode, the output current, output voltage and input impedance can be written as:

$$\begin{cases} I_{\mathrm{oi}} = \omega C_1 U_{\mathrm{in}} \\ U_{oi} = \omega C_1 U_{\mathrm{in}} R \\ Z_{ini} = 1/(\omega^2 C_1^2 R) \end{cases} \tag{12}$$

According to formula (12), in constant current mode, when the system input is a voltage source and the system operating frequency is fixed, the output current is only related to the value of the T-type compensation network capacitance C_1.

C. RESEARCH ON CONSTANT VOLTAGE OUTPUT CHARACTERISTICS

When switch SW_1 is open and SW_2 is closed, the capacitance C_2, C_3, and the inductor L_3 combine to create a π-type equivalent circuit, as shown in Fig.16.

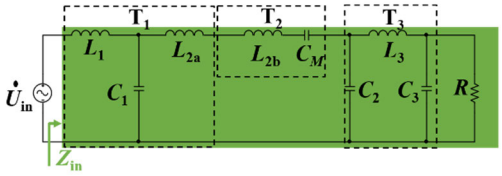

FIGURE 16. Constant voltage circuit.

It can be seen from Chapter III, Section B that the output current I_{oi} is constant, so Fig.16 can be simplified as Fig.17.

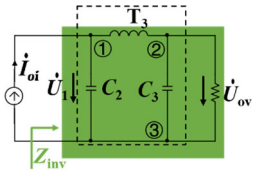

FIGURE 17. Simplified constant voltage circuit.

When the components of T_3 in Fig.17 satisfy formula (13), it can convert a constant input current into a constant output voltage and satisfy the ZPA state.

$$\begin{cases} j\omega L_3 + \dfrac{1}{j\omega C_2} = 0 \\ j\omega L_3 + \dfrac{1}{j\omega C_3} = 0 \end{cases} \tag{13}$$

Taking the ③ node in Fig.17 as a reference point, according to Kirchhoff's current law, the circuit can be written as:

$$\begin{cases} \dot{I}_{oi} = \left(j\omega C_2 + \dfrac{1}{j\omega L_3}\right)\dot{U}_1 - \dfrac{1}{j\omega L_3}\dot{U}_{\mathrm{ov}} \\ 0 = -\dfrac{1}{j\omega L_3}\dot{U}_1 + \left(j\omega C_3 + \dfrac{1}{R}\right)\dot{U}_{\mathrm{ov}} \end{cases} \tag{14}$$

In constant voltage output mode, the output current, output voltage and input impedance can be expressed as:

$$\begin{cases} I_{ov} = I_{oi}/(\omega C_2 R) \\ U_{ov} = I_{oi}/(\omega C_2) \\ Z_{inv} = 1/(\omega^2 C_2^2 R) \end{cases} \tag{15}$$

Combined with formula (12), the output current, output voltage and total input impedance of the system can be obtained:

$$\begin{cases} I_{ov} = U_{in} R C_1/C_2 \\ U_{ov} = U_{in} C_1/C_2 \\ Z_{in} = R C_2^2/C_1^2 \end{cases} \tag{16}$$

According to formula (16), in constant voltage mode, when the system is driven by a voltage source and the system's operating frequency is fixed, the output voltage is only related to the value of the π-type compensation network capacitance C_2.

IV. SIMULATION AND EXPERIMENT

This system operating frequency is 1 MHz, DC input voltage U_{dc} is 100 V, constant current output current is 2 A, constant voltage output is 60 V.

A. SIMULATION ANALYSIS

In order to verify the correctness of the switching method proposed in this paper, a simulation model is built in the Pspice based on the circuit shown in Fig.11 and the components parameters shown in Table.2. The parameters of each component of the system are shown in Table.3.

TABLE 3. Parameter of components.

Component	Value	Components	Value
U_{dc}/V	100	C_3/nF	7.2
f/MHz	1	C_{12}/pF	3.5
L_1/μH	6.1	C_{13}/pF	204
L_2/μH	257.1	C_{14}/pF	0.4
L_3/μH	3.5	C_{23}/pF	0.4
C_1/nF	4.2	C_{24}/pF	202
C_2/nF	7.2	C_{34}/pF	0.6

In this paper, the initial resistance of load is 40 Ω, and the resistance change rate is ±25%. That means the resistance could be 30 Ω, 40 Ω and 50 Ω.

In the 0-t_3 period, SW_1 is closed, SW_2 is opened, and the system is constant current output mode. At times t_1 and t_2, the load resistance increases from 30 Ω to 50 Ω and then decreases to 40 Ω. At time t_3, the system changes to constant voltage output mode. In the 0-tc period, SW_1 is opened, SW_2 is closed, and the system is constant voltage output mode. At times t_a and t_b, the load resistance increases from 30 Ω to 50 Ω and then decreases to 40 Ω. At time t_c, the system changes to constant current output mode. Simulation waveforms of output current in constant current mode and output voltage in constant voltage mode are shown in Fig.18(a) and Fig.18(b) respectively.

From Fig.18(a), it can be seen that at times t_1 and t_2, when the load resistance increases by 67% and then decreases by 20%, the output current remains constant, indicating that the

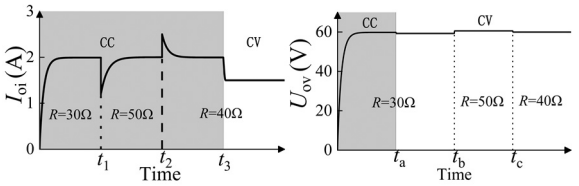

(a) CC output mode (b) CV output mode

FIGURE 18. Simulated waveform.

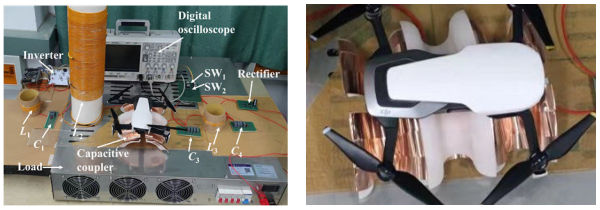

(a) Experimental setup (b) Capacitive coupler

FIGURE 19. Experiment.

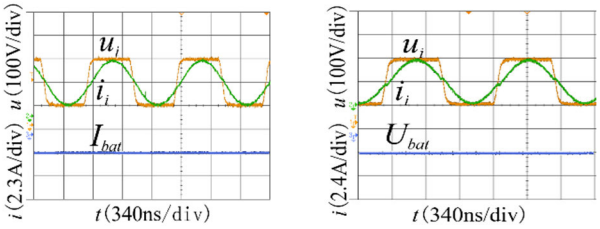

(a) CC mode (b) CV mode

FIGURE 20. Input and output waveform.

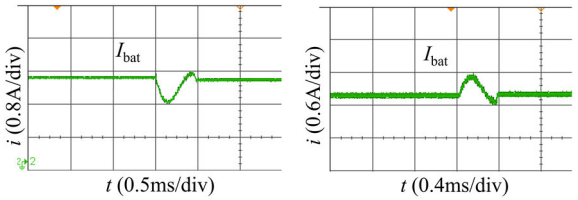

(a) 30 Ω-50 Ω (b) 50 Ω-40 Ω

FIGURE 21. Output waveform of CC mode.

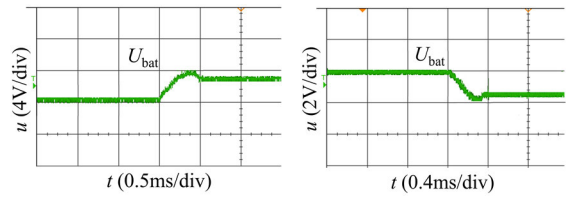

(a) 30 Ω-50 Ω (b) 50 Ω-40 Ω

FIGURE 22. Output waveform of CV mode.

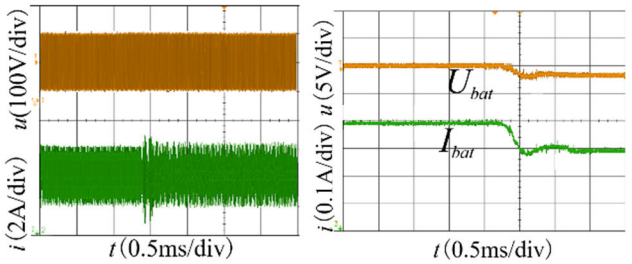

(a) Input voltage and current (b) Output voltage and current

FIGURE 23. Waveform of switching constant current to voltage.

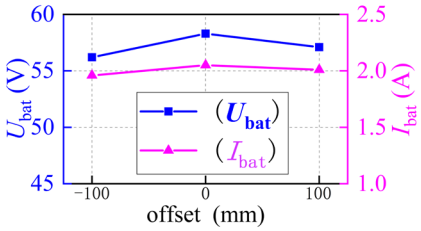

FIGURE 24. The output voltage/current under offset conditions.

system exhibits constant current characteristics. And from Fig.18(b), the system also has constant voltage output characteristics.

B. EXPERIMENT ANALYSIS

Build the test circuit based on the capacitive coupler parameters provided in Table.2 and the component specifications outlined in Table.3, as shown in Fig.19. The transmitter is made of 0.2 mm thick copper strip, and a 1mm thick layer of polytetrafluoroethylene is used as an insulating layer above the emitter electrode plate.

When SW_1 is closed and $SW_2$is opened, the system is CC mode, and when switch SW_1 is opened and SW_2 is closed, the system is CV mode, the waveforms are shown in Fig.20(a) and Fig.20(b), respectively. The output current is 2.1 A in CC mode, voltage is 58 V in CV mode. From Fig.20, it can be seen that the system is in the inductive state, and the input voltage has an approximately zero-phase relationship with the input current.

The output current waveform is shown in Fig.21. From Fig.21(a), it can be seen that when the load changes from 30 Ω to 50 Ω, the output current briefly oscillates with a peak-to-peak value of 0.8 A, before returning to around 2 A. From Fig.21(b), it can be seen that when the load changes from 50 Ω to 40 Ω, the output current remains stable as well. In the two cases above, the rates of change of the output currents are less than 5%.

The output voltage waveform is shown in Fig.22. From Fig.22(a), it can be seen that when the load changes from 30 Ω to 50 Ω, the output voltage changes from 58 V to 61 V. When the load changes from 50 Ω to 40 Ω, the output voltage changes to 59 V in Fig.22(b). In the two cases above, the rates of change of the output voltage are less than 6%.

Fig.23 shows the waveform of the constant current/voltage switching mode. From Fig.23(a) and (b), it can be seen that during the switch period, the input current increases from

TABLE 4. Circuit characteristics.

Literature	[19]	[22]	[18]	This work
Circuit	Fig.26 (a)	Fig.26 (b)	Fig.26 (c)	Fig.13
The number of compensating components of load side	6	5	5	3
The max transition time when load changes in CC mode	0.5 ms	/	25 ms	0.5 ms
The max transition time when load changes in CV mode	2 ms	/	20 ms	0.5 ms
The max change of output current in CC Mode	4%*1 A	5%*1 A	4%*2 A	5%*2 A
The max change of output voltage in CV Mode	4%*50 V	2%*20 V	5%*96 V	6%*60 V
The efficiency in CC mode	≥82%	≥72%	≥80%	≥81%
The efficiency in CV mode	≥85%	≥78%	≥80%	≥76%
ZPA in CC mode	yes	yes	no	yes
ZPA in CV mode	yes	yes	no	yes
The input impedance in CC mode	$\frac{C_{2t}^2}{C_{1t}^2}\times\frac{1}{\omega^2 R}$	$\frac{1}{\omega^2 C_N^2 R}$	$\frac{A+\mathrm{j}B}{C+\mathrm{j}D}$	$\frac{1}{\omega^2 C_1^2 R}$
The input impedance in CV mode	$\frac{C_{2t}^2}{C_{1t}^2}\times\frac{L_{1t}^2}{L_{2t}^2}R$	$\frac{C_3^2}{C_N^2}R$	$\frac{\omega^3 L_t^2 R C_s}{\omega^3 L_t^2 C_s - j(\omega^2(L_t+L_t)C_s+1)}$	$\frac{RC_2^2}{C_1^2}$

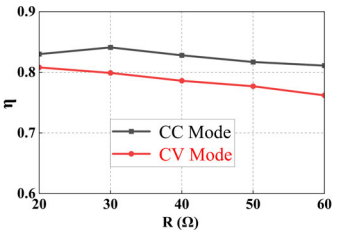

FIGURE 25. Transmission efficiency changes with load.

2.3 A to 2.4 A, and there is a decrease of approximately 4% in the output voltage and current.

The output voltage/current in the case of offset is shown in Fig.24. When the capacitive coupler is offset by ±100mm, the output voltage and current fluctuations are both less than 6%.

Under the given parameter conditions in this paper, the system's transmission efficiency is shown in Fig.25. In CC mode, when the load is 30 Ω, the system efficiency can reach 84%, with the lowest efficiency of the system being 81%. In CV mode, as the load varies from 20 Ω to 60 Ω, the system efficiency gradually decreases but remains above 76%.

C. COMPARISON ANALYSIS

This section provides a comparative analysis of the CPT system of the same type (variable compensation circuit). The related circuits are shown in Fig.26, and the circuit characteristics are shown in Table.4.

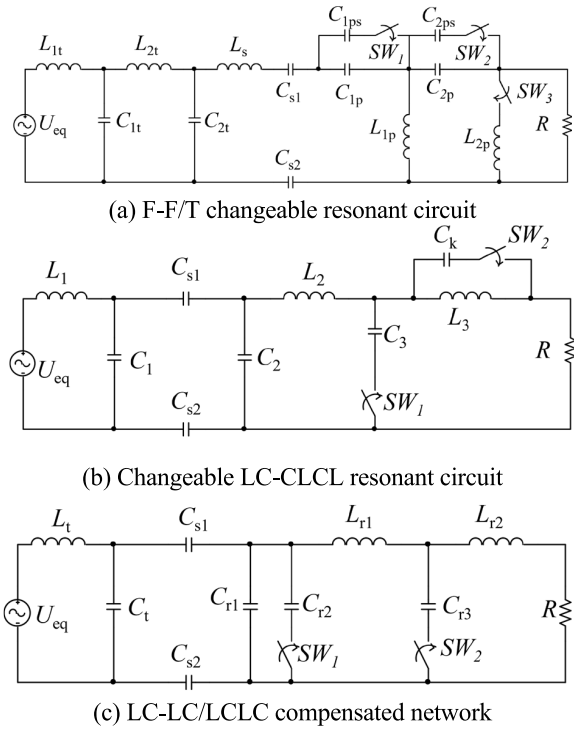

FIGURE 26. The related CPT circuits.

where A, B, C, and D in Table.4 are:

$$\begin{cases} A = (1-(C_r+C_{r3})L_{r2}\omega^2)L_t^2\omega^3 C_s \\ B = L_t^2\omega^4 C_s R(C_r+C_{r3}) \\ C = \omega^3 L_t R(C_r+C_{r3}) + \omega R(C_r+C_{r3}+C_s) \\ D = -1+\omega^4 C_s L_t L_{r2}(C_r+C_{r3}) \\ \qquad +\omega^2(L_{r2}(C_r+C_{r3}+C_s)-L_t C_s) \end{cases}$$

From Table.4, it can be seen that the switching strategy proposed in this paper can ensure that the system is in ZPA state, with minimal voltage/current fluctuations and fluctuation time. Moreover, due to the use of fewer compensation components, it has the advantage of lightweight design.

V. CONCLUSION AND DISCUSSIONS

The main contributions of this article are as follows: the use of fewer compensating components on the load side, improving the lightweight performance of the system; the proposal of a new capacitive coupler with strong anti-offset performance. The capacitive coupler is analyzed based on Maxwell, and the main coupling capacitance and cross-coupling capacitance remained basically unchanged under offset conditions. Based on the designed capacitive coupler, the compensation circuit and switching strategy of CPT system are given, and the simulation model and test prototype are built to verify the effectiveness of the proposed scheme. This CPT system helps to increase the payload capacity of the drone, reduce the precision required for landing, and improve the stability of constant pressure/constant flow output. And the system's efficiency could consistently maintain at over 76%. By using MOSFETs with lower on-state resistance, rectifier diodes with smaller voltage drop, wires with lower resistance, as well as inductors and capacitors with lower resistance, the efficiency of the system can be improved.

The limitations of the proposed system mainly manifest in three aspects:

Resistance to horizontal offset distance: the system has limited resistance to horizontal offset distances along the x and y axes, which are ±54 mm and ±100 mm, respectively.

Resistance to rotational offset distance: the system has a resistance to rotational offset angles of ±23.7°.

The system adopts an open-loop control scheme: when the system's offset distance exceeds the limits mentioned above, or when there are changes in the system's operating frequency, input voltage, etc., closed-loop control needs to be introduced to ensure the stability of the system output.

REFERENCES

[1] Y. Wang, H. Zhang, and F. Lu, "3.5-kW 94.2% DC–DC efficiency capacitive power transfer with zero reactive power circulating," *IEEE Trans. Power Electron.*, vol. 38, no. 2, pp. 1479–1484, Feb. 2023.

[2] M. Z. Erel, K. C. Bayindir, M. T. Aydemir, S. K. Chaudhary, and J. M. Guerrero, "A comprehensive review on wireless capacitive power transfer technology: Fundamentals and applications," *IEEE Access*, vol. 10, pp. 3116–3143, 2022.

[3] Y. Wang, H. Zhang, and F. Lu, "Review, analysis, and design of four basic CPT topologies and the application of high-order compensation networks," *IEEE Trans. Power Electron.*, vol. 37, no. 5, pp. 6181–6193, May 2022.

[4] T. Chen, C. Cheng, H. Cheng, C. Wang, and C. C. Mi, "A multi-load capacitive power relay system with load-independent constant current outputs," *IEEE Trans. Power Electron.*, vol. 37, no. 5, pp. 6144–6155, May 2022.

[5] C. Qi, G. Zheng, Y. Liu, J. Liang, H. Wang, and M. Fu, "A simplified three-order small-signal model for capacitive power transfer system using series compensation," *IEEE Trans. Power Electron.*, vol. 38, no. 5, pp. 5688–5692, May 2023.

[6] X.-Y. Wu, Y.-G. Su, A. P. Hu, L. J. Zou, and Z. Liu, "A sleeve-type capacitive power transfer system with different coupling arrangements for rotary application," *IEEE Access*, vol. 8, pp. 69148–69159, 2020.

[7] Y. Shin, S. Woo, C. Lee, J. Jeong, G. Kwak, and S. Ahn, "Design of a wireless power transfer system with two inputs with large voltage differences for missiles mounted on maritime vessels," *IEEE Access*, vol. 10, pp. 70825–70839, 2022.

[8] B. Regensburger, S. Sinha, A. Kumar, S. Maji, and K. K. Afridi, "High-performance multi-MHz capacitive wireless power transfer system for EV charging utilizing interleaved-foil coupled inductors," *IEEE J. Emerg. Sel. Topics Power Electron.*, vol. 10, no. 1, pp. 35–51, Feb. 2022.

[9] P. K. Chittoor, B. Chokkalingam, and L. Mihet-Popa, "A review on UAV wireless charging: Fundamentals, applications, charging techniques and standards," *IEEE Access*, vol. 9, pp. 69235–69266, 2021.

[10] R. Narayanamoorthi, "Modeling of capacitive resonant wireless power and data transfer to deep biomedical implants," *IEEE Trans. Compon., Packag., Manuf. Technol.*, vol. 9, no. 7, pp. 1253–1263, Jul. 2019.

[11] M. N. Boukoberine, Z. Zhou, and M. Benbouzid, "A critical review on unmanned aerial vehicles power supply and energy management: Solutions, strategies, and prospects," *Appl. Energy*, vol. 255, Dec. 2019, Art. no. 113823.

[12] S. Wu, C. Cai, and T. Chen, "Research progress and development trend of multi-rotor unmanned aerial vehicles wireless charging technology," *Trans. Chin. Electrotech. Soc.*, vol. 37, no. 3, pp. 555–565, 2022.

[13] S. Pahlavan, M. Shooshtari, M. Maleki, and S. J. Ashtiani, "Using overlapped resonators in wireless power transfer for uniform electromagnetic field and removing blank spots in free moving applications," *Electronics*, vol. 11, no. 8, p. 1204, Apr. 2022.

[14] C. Cai, X. Liu, S. Wu, X. Chen, W. Chai, and S. Yang, "A misalignment tolerance and lightweight wireless charging system via reconfigurable capacitive coupling for unmanned aerial vehicle applications," *IEEE Trans. Power Electron.*, vol. 38, no. 1, pp. 22–26, Jan. 2023.

[15] S. Wu, X. Chen, and X. Meng, "An electric-field coupled wireless power transfer system with misalignment-tolerance and light-weight characteristics for unmanned aerial vehicle applications," *Proc. CSEE.*, vol. 43, no. 6, pp. 2404–2413, 2023.

[16] S. Zang, K. Lu, S. K. Nguang, and W. Sun, "Robust H ∞ output feedback control of a rotary capacitive power transfer system," *IEEE Access*, vol. 7, pp. 113452–113462, 2019.

[17] F. Lu, H. Zhang, H. Hofmann, and C. C. Mi, "A double-sided LC-compensation circuit for loosely coupled capacitive power transfer," *IEEE Trans. Power Electron.*, vol. 33, no. 2, pp. 1633–1643, Feb. 2018.

[18] X. Qing, Y. Su, A. P. Hu, Z. Liu, and X. Hou, "A CPT system with switchable compensation for constant current or voltage output against load and coupling capacitance variations," *Electr. Eng.*, vol. 103, no. 5, pp. 2391–2402, Oct. 2021.

[19] S. Yugang, X. Shiyun, and W. Zhihui, "An electric-field coupled power transfer system with constant voltage and constant current output based on F-F/T changeable resonant circuit," *Trans. China Electrotech. Soc.*, vol. 34, no. 6, pp. 1127–1136, 2019.

[20] Z. Liao, L. Zhou, Z. Wu, G. Wei, and C. Xia, "An electric-field coupled power transfer system with constant voltage and constant current output based on changeable LC-CLCL resonant circuit," *Proc. CSEE.*, vol. 41, no. 17, pp. 6039–6050, 2021.

[21] L. Zhao, D. Li, C. Zhao, and F. Jiang, "Some achievements on detection methods of UAV autonomous landing markers," *Chin. J. Aeronaut.*, vol. 43, no. 9, pp. 274–289, 2022.

[22] H. Zhang, F. Lu, H. Hofmann, W. Liu, and C. C. Mi, "A four-plate compact capacitive coupler design and LCL-compensated topology for capacitive power transfer in electric vehicle charging application," *IEEE Trans. Power Electron.*, vol. 31, no. 12, pp. 8541–8551, Dec. 2016.

YUFANG CHANG received the B.E. degree in automation, the M.E. degree in control theory and control engineering, and the Ph.D. degree in traffic information engineering and control from the Wuhan University of Technology, Wuhan, China, in 2001, 2004, and 2013, respectively. She is currently a Professor with the School of Electric and Electrical Engineering, Hubei University of Technology, Wuhan. She has supervised a number of M.S. degree students in the area of control engineering. Her current research interests include system identification, microgrid control systems, and advanced control theory.

XIAOKE ZHANG was born in Henan, China, in 1997. He received the B.S. degree in electrical engineering and automation from the Henan University of Technology, Zhengzhou, Henan. He is currently pursuing the M.S. degree with the Hubei University of Technology. He is also a member of the Research and Development Team of Wireless Power Transfer System. His research interests include the switching strategy of constant voltage/current of the wireless power transfer systems.

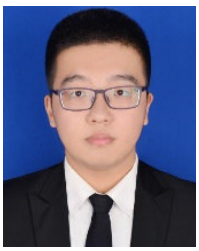

CHAO MA was born in Hebei, China, in 1998. He received the bachelor's degree in electrical engineering and automation from the Hebei University of Science and Technology, where he is currently pursuing the master's degree. He is also a member of the Research and Development Team for Wireless Power Transmission Systems. His research interests include the parameter identification of loads and mutual inductance in wireless power transmission systems.

WENCONG HUANG received the B.E. degree in automatic control, the M.E. degree in control theory and control engineering, and the Ph.D. degree in traffic information engineering and control from the Wuhan University of Technology, Wuhan, China, in 2000, 2006, and 2020, respectively. He is currently an Associate Professor with the School of Electric and Electrical Engineering, Hubei University of Technology, Wuhan. He has supervised a number of M.S. degree students in the area of electrical engineering. His current research interests include computational electromagnetics, wireless power transmission, high-frequency DC/DC converters, and embedded systems.

HUAICHENG YAN (Senior Member, IEEE) received the B.S. degree in automatic control from the Wuhan University of Technology, Wuhan, China, in 2001, and the Ph.D. degree in control theory and control engineering from the Huazhong University of Science and Technology, Wuhan, in 2007. From 2007 to 2009, he was a Postdoctoral Fellow with The Chinese University of Hong Kong, Hong Kong. From June 2011 to August 2011, he was a Research Fellow with The University of Hong Kong, Hong Kong. From February 2012 to August 2012, he was a Research Fellow with the City University of Hong Kong. Currently, he is a Professor with the School of Information Science and Engineering, East China University of Science and Technology, Shanghai, China. His current research interests include the UAV/spacecraft control and artificial intelligence.